Spectral information from photon statistics in x-ray radiography and computed tomography

Qiheng Yang ⓘ, Wilfred Fullagar, Mahsa Paziresh, Glenn Myers, Shane Latham, Adrian Sheppard, and Andrew Kingston ⓘ*

Department of Applied Mathematics, Research School of Physics, The Australian National University, Canberra, ACT 2601, Australia

Measuring spectral information requires distinguishing photons of different energies, typically achieved using filters or advanced detectors sensitive to individual photons. We prove that when the arrival of photons follows a Poisson distribution (i.e., is shot-noise dominated), the variance and mean of the total photon energy collected over a fixed interval provide independent information about the photon energy spectrum. This immediately leads to several striking corollaries. First, the variance data can be used in the same way as the mean data in both x-ray radiography and tomography. Second, the ratio of the variance data and mean data provides an indication of the average energy of the photon spectrum. Third, the variance data, when compared to the mean data, reveal information analogous to using a higher-energy spectrum. These corollaries show that spectral information can be recovered even from common x-ray detectors which only measure aggregate photon energy. As a demonstration, we performed beam-hardening correction in computed tomography using variance data for both simulations and experiments. We also achieved quantitative tomographic reconstruction in simulation and recover accurate attenuation coefficient values in addition to material density and atomic number.

I. INTRODUCTION

The energy of electromagnetic radiation arrives as discrete photons, and the random variations in detection follow shot noise, modeled by the Poisson distribution. For example, a detector may collect n photons in a certain time interval, and repeating this measurement yields an average of $\bar{n}$ photons with variance of $\bar{n}$. The randomness in the arrival of the x-ray photons applies only to the number of photons, which may be due to (1) randomness in the generation of the photon in the x-ray tube, (2) the possible attenuation of the photon en route to the detector, or (3) the likelihood of the x-ray photon being fully stopped inside the detector and registered as a signal. All these processes are probabilistic events which we can combine into one Poisson distribution. The peculiar property of the Poisson distribution where the mean is equal to the variance therefore affects only the photon number at the detector. The mean and variance as measured by a detector do not necessarily obey that equivalence, as the detector reading (of the most common x-ray detectors) is related to the total energy of all the collected photons, i.e., $\sum_i n_i E_i \Gamma(E_i)$, where n_i photons have energy E_i detected with efficiency $\Gamma(E_i)$. This efficiency $\Gamma(E_1)$ applies to photons which are already detected; therefore, it is a fixed value for each energy depending on the detector response, and not a part of the prior statistical considerations. At first glance, it does not appear to be possible to extract information about the energy distribution of the photons when the detector only measures aggregate values. Nonetheless, we note the variance of detector readings provides information distinct from the mean reading, which is $\sum_i \bar{n}_i E_i \Gamma(E_i)$. The photon number n_i is a random variable

that has a Poisson distribution and is independently distributed for each energy i. $E_i \Gamma(E_i)$ is a constant multiple; therefore, the mean detector reading, as a sum of independent scaled Poisson variables, is itself a Poisson variable. We can use the properties of the variance for adding scaled independent distributions to obtain the variance of the detector reading as $\sum_i \bar{n}_i E_i^2 \Gamma^2(E_i)$. The subtle difference between the mean and the variance carries several intriguing implications that will be explored in this paper.

In conventional x-ray computed tomography (XCT), one x-ray radiograph is taken at each orientation with an exposure time sufficiently long enough to detect a statistically meaningful number of x rays. We can also collect many radiographs at the same orientation and calculate mean and variance images. The variance data from polychromatic x-rays provide additional information that can be used to correct beam-hardening artifacts, even when the x-ray spectrum is not known. More specifically, once normalized, the variance data resemble the mean data illuminated with a harder x-ray spectrum: exactly what is required for dual-energy reconstruction. This means that if the x-ray spectrum is known, we can carry out a quantitative, dual-energy-type reconstruction from measured mean and variance data. The practical implications can be considered in three successive stages.

First, the difference between the mean detector reading and the variance detector reading only depends on the x-ray energies, which suggests that a function of the energy can be extracted if both the variance and the mean are known. This is most obvious in the case of monochromatic x rays where there is only one energy, E_0, and the variance is simply the mean scaled by $E_0 \Gamma(E_0)$. Indeed, we have recovered the individual photon energy using a detector that does not distinguish individual photons in Ref. [1]; in that paper we compared the procedure to finding the size of a single raindrop from an array

---

*Corresponding author: andrew.kingston@anu.edu.au

of cups collecting precipitation over a set period, which we also carried out in practice. If the x rays are polychromatic, the analysis is slightly more complicated, but the ratio still yields something useful, as we will demonstrate in Sec. III.

Following this line of inquiry, we consider the possibility that the variance detector reading can be used in the same way as the mean detector reading. Consider a detector array used to record an x-ray radiograph, but each reading is repeated several times so the mean across all the samples is calculated for each pixel. This *mean radiograph* is functionally equivalent to each of the individual radiographs, but what about a similarly constructed *variance radiograph*? The expression we used above suggests that it is also a valid radiograph. Recall the expression $\sum_i n_i E_i \Gamma(E_i)$, which is the aggregate energy measured when n_i photons have energy E_i. Similarly, we can interpret $\sum_i \bar{n}_i E_i^2 \Gamma^2(E_i)$ as the total energy of $\Sigma_i \bar{n}_i$ photons, where $\bar{n}_i$ have energy $E_i^2 \Gamma(E_i)$. Again, this revelation is surprising, but we have confirmed the hypothesis that the variance radiograph is equivalent to a mean radiograph illuminated using a different energy spectrum in both experiment and simulation (see Sec. IV).

Finally, we move from radiographs to a collection of radiographs measured from different viewing directions (i.e., a sinogram) recorded for the purpose of XCT. Since each variance radiograph is in theory equivalent to a radiograph illuminated with a different average energy, this implies that by recording both the variance and the mean, two different sinograms can be obtained for the same experiment using one x-ray spectrum. The mean and variance sinograms can then function as two different scans in dual-energy computed tomography (DECT) reconstruction. This demonstrates that dual-energy XCT can be done *without* the use of spectrum-resolving detectors or two different x-ray spectra deployed either simultaneously or in sequence. We believe this represents an advance in the understanding of x-ray physics which can also be applied in the lab. Quantitative tomographic reconstruction using these concepts is demonstrated in Sec. V using measurements generated by simulation.

Numerous previous works have studied the statistical properties of x-ray photon detection (e.g., Refs. [2–5]). It is even possible to utilize knowledge about x-ray statistics in maximum-likelihood reconstruction methods [6,7]. However, to date we have found no study that specifically attends to the spectrally independent information in the variance of the detector readings, which we exploit fully as a core theme of this paper. For example, a comparison can be made with Ref. [6], in which contemporary Bayesian methods are employed on measurements with two separate x-ray spectra to achieve dual-energy tomographic reconstruction; our approach achieves similar ends using only *one* x-ray spectrum.

Of course, spectrally resolving detectors do exist, and have been slowly revolutionizing x-ray detection. Nevertheless, it is exciting to see that there is still unrealized potential in existing conventional detectors. When choosing an x-ray detector, it is common to put more emphasis on response time and resolution over features such as spectral resolution, which is commonly regarded as a luxury, particularly when taking budgetary constraints in mind. We hope to show that some very helpful spectral measurements can be made even if the original manufacturers of the detector did not anticipate such

capabilities. And we want to provide enough detail to enable others to implement the collection of variance and mean sinograms in experiment and simulation, to verify the relationship between their ratios, and to use them in the suggested beam-hardening correction techniques.

The remainder of the paper proceeds as follows: In Sec. II we introduce the Alvarez-Macovski x-ray attenuation model, which is a function of atomic number, density, as well as x-ray energy. This gives us a method to account for beam-hardening artifacts in iterative tomographic reconstruction algorithms. In Sec. III we provide an analysis of the statistics of x-ray detection for both monochromatic and polychromatic x-ray beams. Here we reveal that the mean and variance of detector readings provide independent data and that meaningful radiography and tomography can be done with the variance data alone. In Sec. IV, we present various proof-of-concept results from both experimental and simulated data. Then, in Sec. V we use the additional information from the variance measurements to correct beam-hardening artifacts and extract material properties such as density and atomic number in simulation when the imaging spectrum is known. Finally, we conclude the paper in Sec. VI and suggest some future research directions made possible by this work.

II. BACKGROUND

We begin by briefly reviewing the basic physics of x-ray production, interaction, and detection. These processes provide an essential foundation for understanding the operation and pitfalls of XCT and also the source of the statistics properties of x-ray detection.

Before beginning the background section proper, we wish to clarify the different meanings when we use the words "average" or "mean," which frequently occur throughout the paper and may be a source of confusion. We hope that the context in which the words are used would be enough to distinguish the meanings. The two main contexts are as follows:

(i) The mean or average energy of a collection of x-ray photons, or the mean energy of the x-ray spectrum, is simply the average energy carried by the x-ray photon or E/n, where E is the total energy of the collection and n the number of photons.

(ii) The mean or average reading of the x-ray detector is the mean of the detector reading when there are repeated measurements of the same event, i.e., R/m where R is the detector reading and m the number of trials.

A. Difficulties in quantitative imaging from x-ray beam hardening

X-ray attenuation represents how strongly an object reduces the intensity of incident x rays through absorption and scattering. The attenuation is not measured directly. Instead, the intensity of the x-ray beam is measured both with (I) and without (I_0) the attenuating object; the ratio of the two is the x-ray transmission. X-ray transmission along a line L at each x-ray energy E is modeled according to the well-known simple attenuation law. This posits an exponential relationship
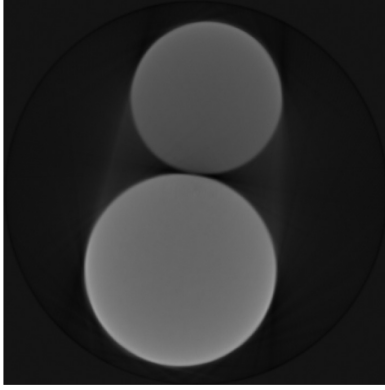
FIG. 1. Two-dimensional slice of experimental data consisting of 8-mm-diam Al rod and 10-mm-diam $CaCO_3$ core. Polychromatic x rays, generated by a W reflection target from a 70-keV electron beam, are filtered by 0.25 mm Al. Grayscale: $[-0.05, 0.35]$.

being the attenuation and intensity, and it has the form

$$I(L; E) = I_0(L; E)D(E) \exp\left(-\int_L \mu(\mathbf{x}; E)\,ds\right), \quad (1)$$

given an incident intensity $I_0(L; E)$ at energy E and a detector efficiency of $D(E)$. Typical laboratory-based x-ray sources produce polychromatic x rays with energy range up to E_a (the accelerating voltage of the x-ray tube multiplied by the electron charge). The total transmitted intensity across all energies is

$$I(L) = \int_0^{E_a} I_0(L; \xi)D(\xi) \exp\left(-\int_L \mu(\mathbf{x}; \xi)\,ds\right) d\xi. \quad (2)$$

We can calculate projected attenuation at energy E directly for monochromatic x rays by 'linearization" using Eq. (1):.

$$\int_L \mu(\mathbf{x}; E)\,ds = -\ln\left(\frac{I(L; E)}{D(E)I_0(L; E)}\right). \quad (3)$$

Polychromatic intensity data cannot be linearized in the same way because the right-hand side of Eq. (2) contains the integral of an exponential, and polychromatic x rays behave in a substantially different way compared to monochromatic x rays. However, in limited cases, such as a single material object, the projected attenuation can be solved through a calibration process. In general, we cannot extract this information from polychromatic intensity measurements alone. The result of this complexity in tomography is *x-ray beam-hardening* artifacts: low-energy x rays are attenuated preferentially, causing the spectral distribution to change as the x-ray beam passes through material. The emerging x-ray beam has a higher average energy (i.e., becomes "harder"; we refer the reader to Sec. 6 of Ref. [8] for a more detailed overview). Figure 1 depicts typical artifacts produced by beam hardening in conventional tomographic reconstruction. The object consists of a marble rod (lower) and an aluminum rod (upper), and an ideal reconstruction should depict uniform gray values inside each of the material, and clear difference between the two rods. Instead, we observe a large distribution of gray values caused by reconstruction artifacts. The two main groups of artifacts are (1) an increase in apparent attenuation towards the boundaries

of the cylinders (cupping) and (2) the smearing of attenuation values in the region between the cylinders (streaking).

In order to utilize Eq. (2), we need to have a model of the energy dependence of x-ray attenuation $\mu(\mathbf{x}; E)$; this is given in the next section.

B. The Alvarez-Macovski (AM) model for x-ray attenuation

The Alvarez-Macovski model is a simple and commonly used x-ray attenuation model valid for typical x-ray energies (around 10–300 keV, which covers the majority of x-ray use cases) [9]. Alvarez and Macovski showed that x-ray attenuation for a material can be reasonably approximated by two basis functions, which are themselves functions of two material properties: density, ρ, and atomic number, Z. It has the form

$$\mu(\mathbf{x}; E) = \frac{Z}{A}\left(\frac{\alpha'}{E^3}\rho(\mathbf{x})Z^3(\mathbf{x}) + \beta' f_{KN}(E)\rho(\mathbf{x})\right),$$

where $\mathbf{x}$ is the [three-dimensional (3D) Cartesian] coordinate, α' and β' are constants, and $f_{KN}(E)$ is the Klein-Nishina function at energy E [10]. For the stable isotopes of most materials, it is reasonable to assume that atomic weight, A, is directly proportional to Z, i.e., $Z(\mathbf{x})/A(\mathbf{x}) \approx 0.5$. We have also found that it is more accurate to set the coefficient of Z in the photoelectric component to 3.2 instead of 3 [11]. By absorbing the approximate ratio into the existing constants of α and β, i.e., setting $\alpha = 0.5\alpha'$ and $\beta = 0.5\beta$, our attenuation model takes the following form:

$$\mu(\mathbf{x}; E) = \frac{\alpha}{E^3}\rho(\mathbf{x})Z^{3.2}(\mathbf{x}) + \beta f_{KN}(E)\rho(\mathbf{x}). \quad (4)$$

The first basis function models photoelectric absorption of x rays, while the second basis function models Compton scattering of x rays. The model is very accurate for materials which contain elements with atomic number less than 20. Since the Alvarez-Macovski model does not take account of K edges, materials with an absorption edge in their attenuation curve in the relevant x-ray energy range may be imperfectly modeled around the point of discontinuity (for a full model of the x-ray attenuation, see, for example, Ref. [12]). Notwithstanding these inaccuracies, we have found that it is also usable even when interaction edges are present because the overall shape of the curve is preserved and the spectrum weighted intensity calculated by the model remained accurate [13]. For most materials both Rayleigh scattering (which does not change the x-ray energy) and pair production can be ignored in typical x-ray energy ranges without greatly impacting the accuracy. Finally, to avoid getting bogged down in the thorny problem of x-ray scattering, we treat scattered x rays as completely lost. In effect, for the duration of this paper we consider x rays as geometric beams which are only attenuated and not deflected.

In XCT it is common to work with the projected attenuation values, which is analogous to the linearized intensity as in Eq. (3). Because the projection operation is a linear process, the total attenuation, or projected attenuation, along a line L is equal to the line integral of the material properties, $\rho(\mathbf{x})$ and

$\rho Z^{3.2}(\mathbf{x})$, along the same line:

$$\int_L \mu(\mathbf{x}; E)\, ds = \frac{\alpha}{E^3} \int_L \rho Z^{3.2}(\mathbf{x})\, ds + \beta f_{KN}(E) \int_L \rho(\mathbf{x})\, ds. \tag{5}$$

For more technical details on line integrals and the projection operation, see Chap. 3 of Ref. [14].

Since the Alvarez-Macovski model has two independent components corresponding to the material properties $\rho(\mathbf{x})$ and $\rho Z^{3.2}(\mathbf{x})$, quantitative reconstruction of x-ray attenuation at arbitrary energies for unknown materials therefore requires two independent measurements. This is usually done in the form of x-ray transmission recorded with two different x-ray spectra, i.e., DECT [15]. We will show that while using only one x-ray spectrum, measuring the mean and variance of the x-ray transmission can also satisfy this requirement, even when using conventional scintillator detectors.

III. STATISTICAL PROPERTIES OF ENERGY-INTEGRATED INTENSITY MEASUREMENTS

A. Motivation

In our opinion, many problems facing XCT, such as beam hardening, are in essence problems of underdetermined systems. The most commonly used reconstruction algorithms can, in theory, produce artifact-free tomograms from monochromatic measured data. However, when polychromatic x rays are employed along with detectors which do not resolve x-ray energy, insufficient information is captured to account for the more complex change in x rays after they pass through the object (this is true in general, although for trivial cases such as single material objects the problems can be more easily dealt with). Conventional wisdom states that scintillators and charge coupled devices (CCDs), among other energy-integrating detectors, do not capture spectral information. We have recently shown that this is not the case, and by utilizing the statistics of incoming x-ray photons, or photon shot noise, the variance and the mean actually carry different information about the x-ray spectrum [1].

B. X-ray intensity mean and variance

Consider a single measurement of x-ray intensity with no attenuating object at a certain detector pixel over a fixed interval. We anticipate intensity I_0, which consists of $N(E)$ discrete x-ray photons at each x-ray energy E. The actual measurement of the x-ray intensity involves several physical processes each with their statistical quirks, along with the necessity of measuring a "dark field" or background reading. However, if we ensure the photon count is high enough then the x-ray statistics should dominate the noise [16]. The energy range of the x rays is between zero and the energy of the electron beam in the x-ray tube, E_a. Finally, the x-ray detector has a certain efficiency of energy throughput, $\Gamma(E)$, which is a real number between zero and 1 for photons with energy E. If this measurement is repeated, the mean, or average, measured intensity over all the observations is

$$\bar{I}_0 = \int_0^{E_a} \langle N(\xi) \rangle \xi \Gamma(\xi)\, d\xi. \tag{6}$$

Note that the detector reading is proportional to the total energy of the incoming x-ray photons, which is true for, among others, scintillators and CCD detectors. The number of detected photons, $N(E)$, like the number of incoming photons, follows the Poisson distribution with mean $\langle N(E) \rangle$; here the angle brackets have their usual meaning of expected value. We assume that we have good knowledge about the spectrum, which will remain unchanged for the same experiment or simulation, and henceforth we treat $\langle N(E) \rangle$ as a constant. Like in Ref. [1], we expect the standard deviation of $N(E)$ to be $\langle N(E) \rangle$ as per the properties of the Poisson distribution. The variance, $\check{I}_0 = \sigma^2(I_0)$, is

$$\check{I}_0 = \int_0^{E_a} \langle N(\xi) \rangle \xi^2 \Gamma^2(\xi)\, d\xi. \tag{7}$$

The choice of notation for the variance here is deliberate, and will be justified in due course. It was shown in Ref. [1] that for the flat panel scintillator detectors in our laboratory $\Gamma(E)$ is roughly constant over the energies delivered by our x-ray source. From here on we will assume that, over the energy range of interest, the detector response as a function of energy, $\Gamma(E)$, can be represented by the constant γ. In the simulations, for simplicity and without loss of generality, γ is set to 1.

C. Determining expected x-ray energy through intensity mean and variance

Dividing the variance of the incident radiation by its mean, $\check{I}_0/\bar{I}_0$, gives [1]

$$\check{I}_0/\bar{I}_0 = \gamma \int_0^{E_a} \xi S_0(\xi)\, d\xi = \gamma \, \text{Mean}\,[S_0], \tag{8}$$

where S_0 is the spectral distribution (or probability density function) of the incident radiation S_0, i.e.,

$$S_0(E) = \frac{\langle N(E) \rangle E}{\int_0^{E_a} \langle N(\xi) \rangle \xi \, d\xi}.$$

$S_0(E)$ measures the proportion of total energy in the x-ray beam that is comprised of photons with energy E. Let Mean[·] denote the expected value as a weighted sum, i.e., $\text{Mean}[S_0] = \int_0^{E_a} \xi S_0(\xi)\, d\xi$. The expression $\text{Mean}[S_0]$ is the mean energy of the spectrum. This value increases when the beam is hardened or the accelerating voltage of the x-ray tube is increased.

The expected energy of the spectrum is extremely valuable data. We have essentially extracted spectral information from an intensity integrating detector which should not have any such capabilities. Simply by using x-ray statistics, this shows that each individual detector pixel in effect "sees" a different x-ray spectrum (which we can calculate). Since the effects of beam-hardening artifacts are precisely due to this shift in x-ray spectrum, we now have a promising avenue of doing beam-hardening artifact correction. Before diving into the details, let us first explore some of the properties of the transmission variance.

D. Transmitted intensity mean and variance

Now consider a specimen with attenuation coefficient of $\mu(\mathbf{x}, E)$ at coordinate $\mathbf{x}$. The intensity measured from the

same detector pixel in the same time interval with this specimen in front of the detector is given in Eq. (2). The mean $\overline{I}(L)$ can then be found by substituting the incident illumination with Eq. (6) to give

$$\overline{I}(L) = \gamma \int_0^{E_a} \langle N(\xi) \rangle \xi \exp\left(-\int_L \mu(\mathbf{x}, \xi)\, ds\right) d\xi. \quad (9)$$

Since it is the photons of the incident radiation that are stochastically removed by the specimen, we have simply substituted $\langle N(\xi) \rangle$ in Eq. (6) with $\langle N(\xi) \rangle \exp\left(-\int_L \mu(\mathbf{x}, E)\, ds\right)$. The variance is modeled similarly:

$$\breve{I}(L) = \gamma^2 \int_0^{E_a} \langle N(\xi) \rangle \xi^2 \exp\left(-\int_L \mu(\mathbf{x}, \xi)\, ds\right) d\xi. \quad (10)$$

Observe that the variance measurement has a very similar form to the mean measurement. Transmission is simply the ratio of two intensities. Given transmission measurement $T(L) = I(L)/I_0(L)$, the mean is

$$\overline{T}(L) = \int_0^{E_a} \frac{\langle N(\xi) \rangle \xi}{\int_0^{E_a} \langle N(\xi') \rangle \xi'\, d\xi'} \exp\left(-\int_L \mu(\mathbf{x}, \xi)\, ds\right) d\xi$$

$$= \int_0^{E_a} \overline{S}(\xi) \exp\left(-\int_L \mu(\mathbf{x}, \xi)\, ds\right) d\xi, \quad (11)$$

where $\overline{S}$ is the spectral distribution of the radiation as measured at the detector, i.e., $\overline{S}(E) \equiv S_0(E)$. Similarly the variance is

$$\breve{T}(L) = \int_0^{E_a} \frac{\langle N(\xi) \rangle \xi^2}{\int_0^{E_a} \langle N(\xi') \rangle \xi'^2\, d\xi'} \exp\left(-\int_L \mu(\mathbf{x}, \xi)\, ds\right) d\xi$$

$$= \int_0^{E_a} \breve{S}(\xi) \exp\left(-\int_L \mu(\mathbf{x}, \xi)\, ds\right) d\xi, \quad (12)$$

where $\breve{S}$ is again a spectral distribution at the detector which can be written in terms of $\overline{S}$:

$$\breve{S}(E) = \frac{\overline{S}(E) E}{\int_0^{E_a} \overline{S}(\xi) \xi\, d\xi}. \quad (13)$$

Note the similarity between $\breve{T}(L)$ and $\overline{T}(L)$. The two are identical apart from having different spectral distribution functions. Since there is obviously no objection in using the mean measurement in tomography, why not also use the variance measurement? We will pursue this possibility in the following section.

IV. VARIANCE RADIOGRAPHY AND TOMOGRAPHY IN PRACTICE

In the previous section, we presented several theoretical properties of transmission variance in comparison with transmission mean. Before moving on to the direct application of transmission variance in XCT to correct for artifacts (see Sec. V), we will first explain the methods employed to obtain mean and variance data in both simulation and experiment. Then, we will present examples which illustrate some of the basic properties of the transmission variance.
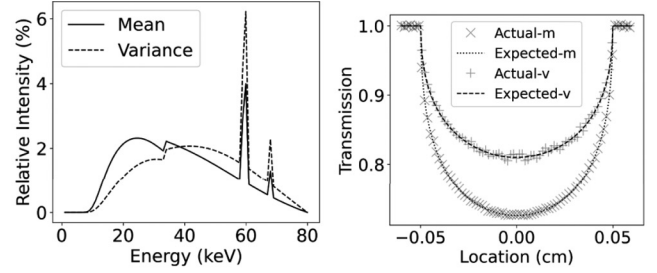
(a) x-ray spectrum

(b) Transmission line profile
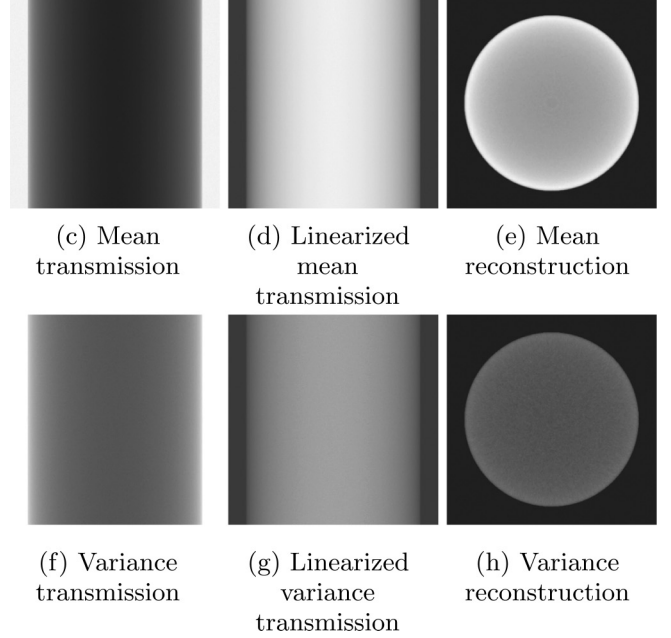
(c) Mean transmission

(d) Linearized mean transmission

(e) Mean reconstruction

(f) Variance transmission

(g) Linearized variance transmission

(h) Variance reconstruction

FIG. 2. (a) The mean spectrum ($\overline{S}$, solid line) and effective variance spectrum ($\breve{S}$, dashed line) used in the simulation. Both spectra are normalized so their distribution functions sum to 1. (b) Line profile of mean and variance transmission for the simulated aluminum circle. (c) Mean transmission, $\overline{T}$, and (f) variance transmission, $\breve{T}$, projection images of the aluminium rod; grayscale is [0.72, 1.0] for both. (d) Mean projected attenuation, $\overline{P}$, and (g) variance projected attenuation, $\breve{P}$; grayscale is [−0.06, 0.33] for both. The tomographic reconstruction of (e) *linearized* mean transmission, $-\ln(\overline{T})$, and (h) *linearized* variance transmission, $-\ln(\breve{T})$; grayscale is [1.17, 3.97] for both.

A. Methods

We begin with Monte Carlo simulations using two-dimensional (2D) phantoms and a line detector: the sinograms are a collection of these lines, and the reconstruction is a 2D image. The sample used in this section for simulations consists of a single 1-mm-diam aluminum rod, imaged with parallel beam x rays produced from a tungsten target. The accelerating voltage of the x-ray source was set to 80 keV and there were no additional filters [the spectrum is given in Fig. 2(a)]. Projection images were simulated at 800 angles with a 400-pixel line detector with a pixel pitch of 15 μm. For each set of one-dimensional (1D) projections, 100 trials are conducted, and the mean and variance data calculated from the trials on the fly using mean absolute deviation (details

outlined in Appendix B). In each trial, a random number of photons is generated and attenuated using the NIST XCOM attenuation data [12], and the emerging photons are recorded for each detector pixel. The photon number follows the Poisson distribution with mean of 10 000. Finally, the 400 × 400 pixel reconstructed tomogram has dimensions 0.6 × 0.6 mm^2.

A marble and aluminum specimen has been used in experiments throughout this paper. It consists of a 10-mm-diam marble (CaCO$_3$) core and an 8-mm-diam aluminum (Al) rod. The specimen was placed 40 mm from a microfocus x-ray source that used a tungsten reflection target, and the illumination of the x-ray source was continuous during the experiment. The accelerating voltage of the x-ray source was set to 70 keV with an electron current of 120 μA and a beam filter of 0.25 mm Al. A Pixium flat-panel detector was placed 786 mm from the source and binned to 360 × 360 square pixels with side length 1.18 mm [17]. A model of the resulting x-ray spectrum as seen by the detector is presented in Fig. 3(a). The detector was set to a frame rate of two frames per second (0.5 s exposure time) with mean and variance images determined from 240 frames. Note that the variance images were calculated using mean absolute deviation which is robust and *on the fly*. Four *dark-field* and eight *clear-field* mean and variance images were collected, along with 360 transmitted intensity mean and variance images collected in a circular trajectory around the specimen captured at 1° intervals.

B. Radiography with intensity variance

The spectral distributions $\overline{S}$ and $\check{S}$ for the simulation are given in Fig. 2(a), where Mean[$\overline{S}(E)$] = 37.9 keV and Mean[$\check{S}(E)$] = 42.3 keV. The entire collection of transmission data from the simulations is presented as sinograms in Figs. 2(c) and 2(f); the corresponding projected attenuation data are shown in Figs. 2(d) and 2(g). We note that the mean [Fig. 2(c)] and variance [Fig. 2(f)] sinograms are very similar, in line with our prediction in Sec. III D. Also notable is the variance sinogram, $\check{T}$, being much noisier than the mean sinogram, $\overline{T}$. This is due to the uncertainty (or standard deviation) in mean scaling approximately as $\sqrt{\lambda/m}$ for expected value λ and m measurements while the uncertainty in variances scales approximately as $\sqrt{2\lambda^2/m}$ (see pp. 313–314 of Ref. [18]).

The simulation data also matched our quantitative predictions. We can calculate beforehand the intensity of the x-ray beam emerging from an object given the x-ray attenuation of the object, the x-ray path length through the object, and the x-ray spectrum. For the Monte Carlo simulation: attenuation data comes from the NIST XCOM database; x-ray path length comes from sample geometry of a circle; and the spectrum is either $\overline{S}$ or $\check{S}$, with the variance spectrum $\check{S}$ calculated using Eq. (13). The theoretical line profile across the transmission images can then be calculated and compared against the actual line profile of the simulated samples; the result is given in Fig. 2(b). Here we observe very good agreement between the theoretical (lower, dotted line) and Monte Carlo ("×") values for the mean transmission; this merely confirms the simulation has been carried out on the correct materials using the correct spectrum. More importantly, there is a close match between the values of the theoretical (upper, dashed line)
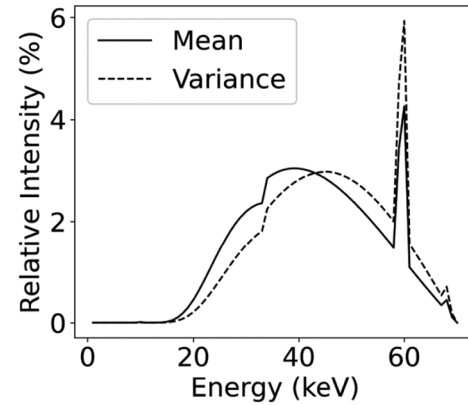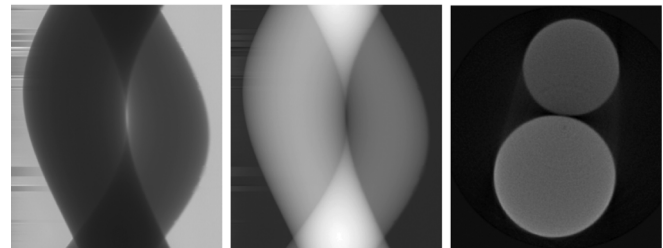

(a) x-ray spectrum
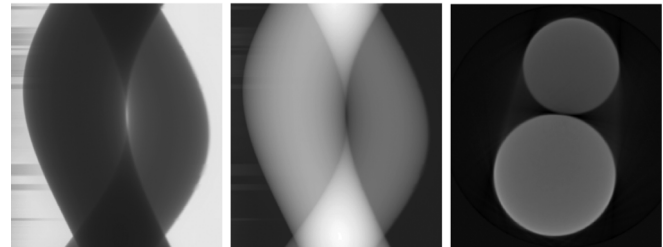
(b) Mean transmission   (c) Linearized mean transmission   (d) Mean reconstruction

(e) Variance transmission   (f) Linearized variance transmission   (g) Variance reconstruction

FIG. 3. (a) The mean spectrum ($\overline{S}$, solid line) and effective variance spectrum ($\check{S}$, dashed line) used in the experimental specimen. Both spectra are normalized so their distribution functions sum to 1. (b) Central slice of the transmission mean, $\overline{T}$, and (e) transmission variance, $\check{T}$, of the specimen described in Fig. 1; grayscale is [0,1.1] for both. (c) Mean projected attenuation, $\overline{P}$, and (f) variance projected attenuation, $\check{P}$, images of the specimen described in Fig. 1; grayscale is [0,4] for both. (d) Central horizontal slice through the tomographic reconstruction of *linearized* mean transmission, $-\ln(\overline{T})$, and (g) variance transmission, $-\ln(\check{T})$. Reconstruction performed using filtered back-projection; grayscale is [−0.05, 0.35] for both. The horizontal streaks visible at the left corners of (b), (e), (d), and (g) are artifacts of unknown cause recorded by the detector. N.B. The experiment utilizes a fan beam, so the transmission images look slightly distorted towards the edges.

and Monte Carlo ("+") values for the variance transmission. The two theoretical line profiles, which are calculated from Eqs. (11) and (12), differ only in the x-ray spectrum, so the close agreement of the Monte Carlo results supports our claim

in Sec. III D that the transmission variance is equivalent to a (noisier) transmission mean but with a harder x-ray spectrum.

Experimental results have been included in Fig. 3 to validate the concept under realistic conditions where there are potentially other contributions to the intensity distribution model, in particular scatter. The spectral distributions modeled for the case-study experiment, $\overline{S}$ and $\check{S}$, are given in Fig. 3(a), where $\text{Mean}[\overline{S}(E)] = 38.5$ keV and $\text{Mean}[\check{S}(E)] = 40$ keV. Example transmission images from the experiment are presented in Figs. 3(b) (Mean) and 3(e), with the corresponding projected attenuation images shown in Figs. 3(c) (Mean) and 3(f). Again the mean and variance images are very similar to the variance data being slightly more noisy and having lower contrast; this is in line with the results of the Monte Carlo simulation and also confirms our prediction in Sec. III D.

C. Tomography with intensity variance

If transmission variance can be considered similar to transmission mean but with a harder spectrum, we should be able to carry out tomographic reconstruction on both data sets. By making the conventional monochromatic assumption, we first linearize the mean polychromatic transmission data as $\overline{P}(L) = -\ln(\overline{T}(L))$, and also linearize the variance data as $\check{P}(L) = -\ln(\check{T}(L))$. A tomogram of the specimen can then be constructed using filtered back-projection, Fourier inversion, or some iterative algebraic scheme.

Tomographic reconstruction has been performed on both the mean and variance data for the Monte Carlo simulation [see Figs. 2(e) and 2(h)] and the case-study experiment [see Figs. 3(d) and 3(g)]. Reconstruction for the simulated data used 25 iterations of the ordered-subset maximum-likelihood for transmission (OSMLTR) algorithm [19,20] and reconstruction of the experimental data used filtered back-projection (FBP). We observe the following: (i) meaningful images are reconstructed from the variance data, demonstrating that variance can be considered in a similar fashion to mean data; (ii) reconstructed attenuation values are slightly lower for the variance data; and (iii) although beam-hardening artifacts (described earlier) are present in both cases they are less significant for the variance data. We interpret observations (ii) and (iii) as evidence that variance measurements have a slightly harder spectrum and a higher expected energy than the mean measurements (i.e., $\text{Mean}[\check{S}(E)] > \text{Mean}[\overline{S}(E)]$).

The properties of variance data in intensity measurements conform to our expectations. In other words, the variance data provide additional information about the specimen which is equivalent to illumination with a different x-ray spectrum. In the next section we will explore some of the potential applications of this additional information in the context of XCT.

V. APPLICATIONS OF STATISTICAL VARIANCE IN COMPUTED TOMOGRAPHY

We have shown that the variance transmission provides another independent set of information about the object. Now we will present several applications utilizing this knowledge which make XCT more quantitative. The ratio of mean and variance transmission data is the average energy of each x-ray beam which passed through the object; it is therefore a direct measure of x-ray beam hardening. Given knowledge of the input spectrum, this enables the distribution of material properties Z and ρ to be determined analogously to dual-energy computed tomography. In what follows, we present these concepts in steps of increasing complexity, proceeding from monochromatic, through bichromatic, and ending with polychromatic spectra.

A. Determining x-ray energy of monochromatic illumination

In the monochromatic case, all incoming x rays are at a single energy E_0; the spectral distribution is the Dirac delta function: $S_0(E) = \delta(E - E_0)$. The variance-mean ratio of the intensities [Eq. (14)] immediately produces the energy of the x rays:

$$\check{I}/\overline{I} = \gamma E_0.$$

1. Methods

The 2D Monte Carlo simulation in this section was carried out by illuminating cylindrical rods of aluminum and marble with radii 0.5 mm using 40-keV x-ray photons in a parallel beam configuration. The attenuation data are taken from the NIST-XCOM database [12]. A 1000-pixel-wide detector was simulated with measurements recorded from 2000 viewing angles. At each angle, each detector pixel was illuminated with an average of 10 000 photons in total in each exposure, and a total of 500 exposures were taken for each angle, and the variance and mean calculated from those exposures on the fly using the mean absolute deviation.

2. Results

The mean and variance intensity images are given in Fig. 4. The variance transmission image [Fig. 4(a)] divided by the mean transmission image [Fig. 4(b)] gives the ratio image [Fig. 4(c)]. The ratio image does not have any features, and its histogram [Fig. 4(d)] gives a normal distribution with mean of 40, which is the energy of the x rays in keV (indicated by the vertical line in the histogram). Note that the ratio image seems noisy everywhere, but the mean and variance intensity seem to have no noise in the regions where transmission is complete (i.e., have values of 1). It is difficult to see in the intensity images, but the regions where transmission is not hindered by the object are still subject to random variation of the photon numbers, and the ratio of the raw variance photon count divided by the raw mean photon count contains lots of noise in that region.

Since the variance transmission is simply a multiple of the mean transmission, although we can extract the x-ray energy directly, there is not much else we can do in this case because no independent information is provided by the variance. Admittedly since only x rays at a single energy are used, no beam-hardening artifacts would appear in the reconstruction, and extraction of further quantitative information is unnecessary in this case.
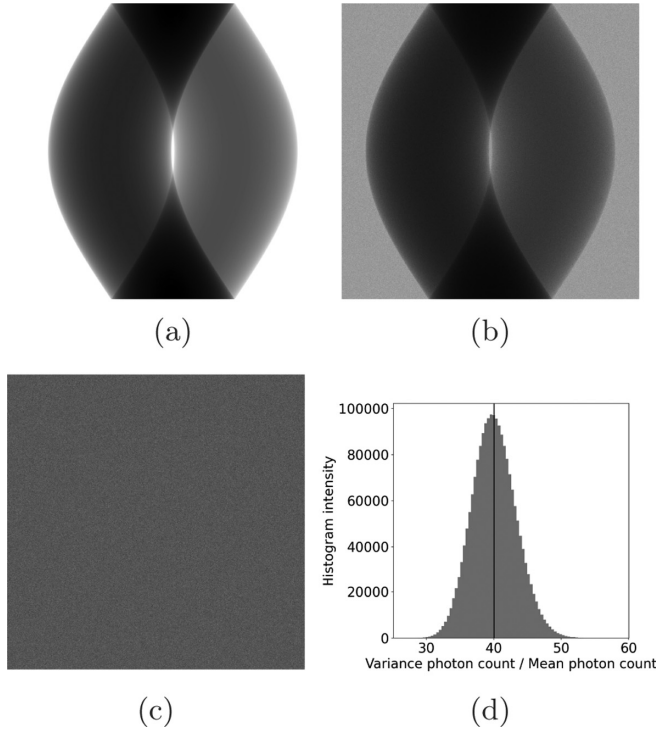
(a)　　　　　　　　(b)

(c)　　　　　　　　(d)

FIG. 4. (a) Mean intensity, grayscale [56473, 400890], and (b) variance intensity, grayscale [1633641, 23069099]; projection images of monochromatic simulation. Their ratio is given in (c), grayscale [58.5, 26.7]. (d) Histogram of the ratio; the vertical line indicates the energy of the x rays.

B. Beam-hardening correction using variance without knowledge of the spectrum

1. Methods

Before proceeding to quantitative reconstruction, we show that it is possible to visualize beam hardening directly using the mean and variance data. This is an extension of the procedure carried out in the previous section (Sec. V A), where only monochromatic x rays are used. Here we use polychromatic x rays to obtain more interesting results. The same case-study experimental data from Sec. IV will be used here (details can be found in Sec. IV A). The same simulated data from the polychromatic illumination (variance transmission and mean transmission from Sec. V C 2) is used as the Monte Carlo simulated sample. A similar analysis was pursued in Sec. 4.1 of Ref. [1].

2. Directly measuring beam hardening (expected x-ray energy) through transmitted intensity mean and variance

Analyzing the polychromatic x rays after transmission through the object, we divide the variance by the mean of the transmitted intensity, $\check{I}/\overline{I}$, to obtain

$$\check{I}/\overline{I} = \gamma \int_0^{E_a} \xi S(\xi) \, d\xi = \gamma \, \text{Mean} \, [S(E)]. \tag{14}$$

We have seen from Sec. V A that Mean[$S(E)$] is the expected energy of the spectral intensity $S(E)$, or the spectrum of the x

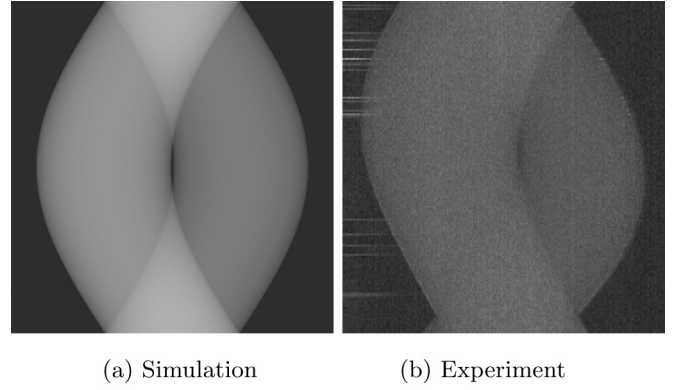
(a) Simulation　　　　(b) Experiment

FIG. 5. (a) The relative change in expected x-ray energy through the simulation specimen; grayscale is [0.91, 1.57]. (b) The relative change in expected x-ray energy through the center of the specimen described in Fig. 1; grayscale is [0.91, 1.57]. The horizontal streak artifacts mentioned in Fig. 3 are also visible in (a) here.

ray that has passed through the object, where

$$S(E) = \frac{\langle N(E) \rangle \exp\left(-\int_L \mu(\mathbf{x}, E) \, ds\right)}{\int_0^{E_a} \langle N(\xi) \rangle \xi \exp\left(-\int_L \mu(\mathbf{x}, \xi) \, ds\right) d\xi}.$$

The change in the expected energy compared to the incident x-ray spectrum $S_0(E)$ gives an indication of the degree of beam hardening that has occurred. The relative change in energy can be obtained without calibration of the detector, since it is simply a ratio of the transmission, i.e.,

$$\frac{\check{I}/\overline{I}}{\check{I}_0/\overline{I}_0} = \frac{\check{T}}{\overline{T}} = \frac{\text{Mean} \, [S(E)]}{\text{Mean} \, [S_0(E)]}. \tag{15}$$

The relative change in expected x-ray energy after passing through the experimental marble and aluminum specimen is presented in Fig. 5(b), and similarly for the Monte Carlo simulation data in Fig. 5(a) (note that the Monte Carlo data contain all of the 1D slices since it is a 2D simulation, and the experimental data consist of one slice of a collection of 2D radiographs). These images are direct depictions of *beam hardening*, i.e., the increase in average x-ray energy after passing the specimen. There is no change in energy on either side of the specimen where $\check{T}/\overline{T} = 1$. Inside the specimen, transmission through the sample causes $\check{T}/\overline{T}$ to increase as some function of the projected attenuation.

Figure 5 shows that we can actually quantify the amount of beam hardening that has occurred by measuring the variance as well as the mean. The next two sections outline automated methods to correct for beam hardening using this information without knowledge of the spectrum. They were first presented in Ref. [21] but here we expand on the methodology.

3. Photoelectric absorption model for x-ray attenuation

As demonstrated in Ref. [13], simplified forms of the AM model that rely on only a single material property are often useful. A common simplification that is appropriate for high-Z material specimens and/or a soft x-ray spectrum is assuming attenuation is dominated by photoelectric absorption, i.e., $\beta =$

0. Projected attenuation then simplifies to the following:

$$\int_L \mu(\mathbf{x};E)\,ds = \frac{\alpha}{E^3}\int_L \rho Z^{3.2}(\mathbf{x})\,ds, \qquad (16)$$

and we observe that the projected attenuation at a specified x-ray energy E_0 can be determined from the projected attenuation at any other energy E as

$$\int_L \mu(\mathbf{x};E_0)\,ds = \frac{E^3}{E_0^3}\int_L \mu(\mathbf{x};E)\,ds. \qquad (17)$$

We now use this simplification as part of a linearization correction using the variance data.

### 4. Correction assuming attenuation is from photoelectric absorption only

Since beam hardening is directly measured by the variance-mean ratio on a per detector pixel basis, we can use this information to reduce the effect of beam-hardening artifacts. Beam hardening is particularly conspicuous when the x-ray spectrum includes energies where x-ray attenuation of the specimen is dominated by photoelectric absorption (PA). Attenuation due to PA is inversely proportional to energy cubed and therefore changes significantly across the spectrum (compared to Compton scattering, which varies much less over the same energies). We can therefore adopt the PA model by itself [Eq. (16)] for x-ray attenuation in this case. Assuming this model, Eq. (17) shows how the attenuation at desired energy E_0 can be computed from the attenuation at energy E. Substituting Eq. (15) into this and assuming $-\ln(\overline{T}(L)) \approx \int_L \mu(\mathbf{x};E)\,ds$ we obtain

$$\int_L \mu(\mathbf{x};E_0)\,ds \approx -\left(\frac{\check{T}(L)}{\overline{\overline{T}}(L)}\right)^3 \ln(\overline{T}(L)). \qquad (18)$$

We carried out 2D FBP reconstruction on simulated data and 3D Feldkamp-Davis-Kress (FDK) reconstruction on experimental data on aluminum and marble rods; the results are given in Fig. 6. The results of applying the variance-to-mean ratio correction directly to the mean attenuation measurements of the simulation data are presented in Fig. 6(c) and the results for the experimental marble and aluminum specimen are presented in Fig. 6(f). Note that this requires no knowledge of the x-ray spectrum. The correction has improved the reconstruction in a qualitative manner: when compared to the uncorrected results [Figs. 6(b) and Fig. 6(e), respectively], the cupping and streaking artifacts have been significantly reduced and the contrast between the materials has improved. On the other hand, there is a slight increase in noise in the corrected result for the Monte Carlo data, and the corresponding result for the experiment is also quite noisy and contains ring artifacts.

5. Correction by a self-calibrated linearization curve

If the direct application of the method outlined previously (Sec. V B 4) is too noisy, we can still use the variance-to-mean ratio as an objective function to calibrate a linearization curve. A well-known method to correct for beam hardening is to apply a *linearization* curve that remaps measured projected attenuation values to the corresponding monochromatic projected attenuation values. This remapping function can be
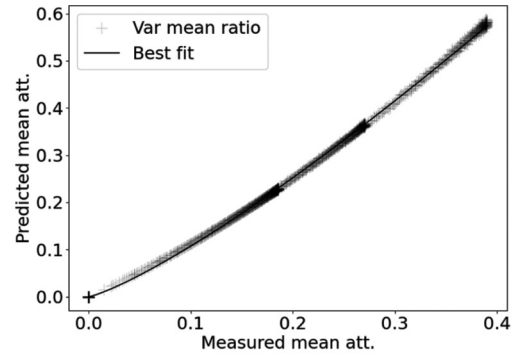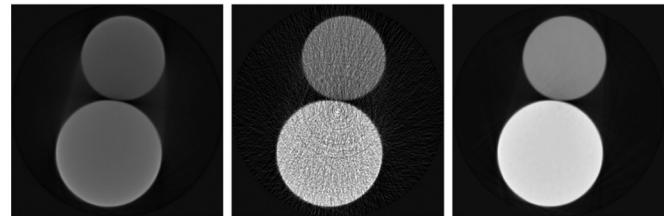

(a) Linearization curve
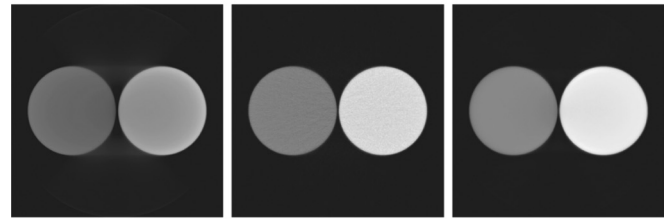
(b) No correction　(c) Correction using variance mean ratio directly　(d) Correction using linearization coefficients obtained from the variance mean ratio

(e) No correction　(f) Correction using variance mean ratio directly　(g) Correction using linearization coefficients obtained from the variance mean ratio

FIG. 6. (a) Linearization curve for the simulation. Row 2: Tomographic reconstruction of the Monte Carlo simulated data, reconstructed from mean transmission, $-\ln(\overline{T})$. (b) Uncorrected, (c) beam hardening corrected according to Eq. (18), and (d) beam hardening corrected using power-law linearization curve: $1.83[\overline{P}(L)]^{1.23}$; grayscale is [0.0, 9.6]. Row 3: Central horizontal slices through the tomographic reconstruction of the experimental specimen, reconstructed from mean transmission, $-\ln(\overline{T})$. (e) Uncorrected, (f) beam hardening corrected according to Eq. (18), and (g) beam hardening corrected using power-law linearization curve: $1.39[\overline{P}(L)]^{1.25}$. Reconstruction is performed using filtered back-projection; grayscale is [−0.05, 0.35].

calibrated using a phantom such as a step wedge; projected attenuation should increase linearly with projected thickness of the phantom. The downside is that calibration phantoms are typically composed of a single material and may not be representative of the specimen being imaged. Fortunately, the variance-to-mean ratio is able to provide exactly this

information. Approximating Eq. (18) as

$$\overline{P}^*(L) = \left(\check{T}(L)/\overline{T}(L)\right)^3 \overline{P}(L),$$

where $\overline{P}^*(L)$ is the corrected, pseudomonochromatic projected attenuation, and $\overline{P}(L)$ is the linearized measurement, i.e., polychromatic projected attenuation, we see that this provides the mapping objective, i.e., an estimate of the projected attenuation at the expected energy of the input spectrum. Now we need a function that maps $\overline{P}(L)$ to $\overline{P}'(L)$ and minimizes the difference from the objective estimate $||\overline{P}'(L) - \overline{P}^*(L)||$, over all lines L. For example, a power-law linearization function defined as $\overline{P}'(L) = A[\overline{P}(L)]^n$ can be used, as it is often quite effective with minimal parameters. The object itself can then be used for parameter calibration as follows:

$$\arg\min_{A,n} \left\| A[\overline{\mathbf{P}}]^n - \left(\frac{\check{\mathbf{T}}}{\overline{\overline{\mathbf{T}}}}\right)^3 \overline{\mathbf{P}} \right\|_2.$$

This technique was applied to both the simulated and case-study experimental marble and aluminum specimens. It was found that $A = 1.83$ and $n = 1.23$ minimized the squared residual for the simulation. A graph of the linearization curve for the simulation is given in Fig. 6(a), with the measured attenuation in the x axis, and the corrected attenuation for the mean-variance ratio $[(\check{\mathbf{T}})(L)/\overline{\mathbf{T}}(L))\overline{\mathbf{P}}(L)]$ is plotted as "+", and the best fit $A[\overline{\mathbf{P}}]^n$ is given by the solid line. For the case-study experimental data, $A = 1.39$ and $n = 1.25$ minimized the squared residual. The result of tomographic reconstruction of the linearized beam-hardened projected attenuation data, $A[\overline{P}(L)]^n$, is presented in Fig. 6(d) for the simulation and Fig. 6(g) for the experiment. By using the power-law linearization, we observe the suppression of cupping and streaking artifacts as well as improved contrast between materials without introducing noise or ring artifacts.

C. Obtaining material properties with knowledge of the spectrum

1. Bichromatic illumination

We return to dual-energy reconstruction using variance in this section. Given knowledge of the spectrum, we can extract more value from the variance data. We will begin with the case of bichromatic illumination where the the x-ray spectrum consist of two energy bins, E_0 and E_1. We introduce this example for pedagogical purposes, since it is not very realistic, but we hope it bridges the gap between monochromatic x rays and polychromatic x rays proper. First, we carry out the same simulation as in Sec. V A on the aluminum and marble rod, except we have changed the x-ray spectrum to a bichromatic spectrum with equal intensity at 30 and 60 keV. The variance, mean transmission, and their ratio are given in Fig. 7. Since the proportion of x rays in each energy bin is different when comparing the variance and the mean transmission [cf. Fig. 2(a)], the ratio of the transmission variance and mean is no longer constant as it was in the monochromatic case presented in Sec. V A, and we observe features corresponding to the object [see Fig. 7(c)]. Note the contrast between this and the uniform image seen in the monochromatic case [Fig. 4(c)]. The histogram [Fig. 7(d)] also has a more complicated shape.
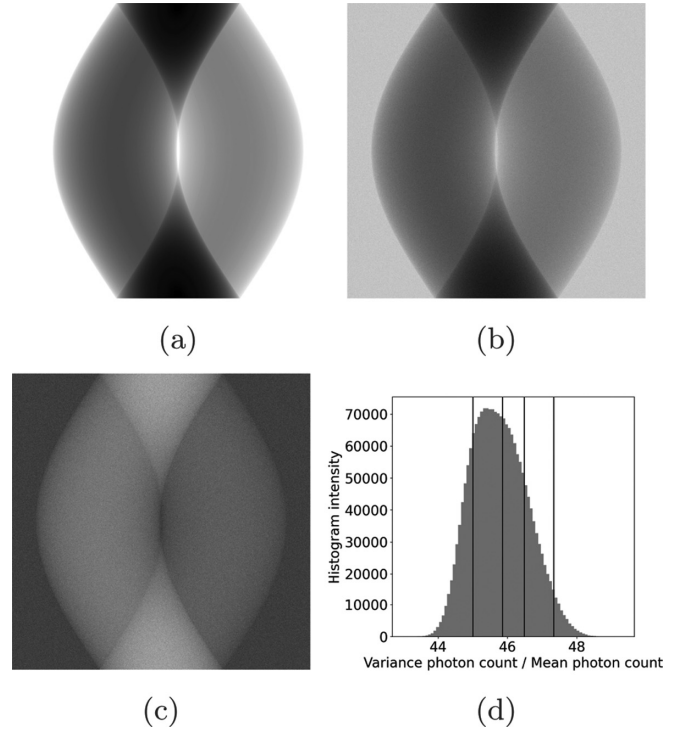

FIG. 7. (a) Mean intensity, grayscale [316961, 400139], and (b) variance intensity, grayscale [14435468, 18827561], projection images of bichromatic simulation. Their ratio is given in (c), grayscale [42.0, 49.3]. (d) Histogram of the ratio, from left to right; the lines indicate the mean energy of the x rays that (1) did not pass through the object, (2) passed through the center of the aluminum, (3) passed through the center of the marble, and (4) passed through the center of both the aluminum and marble.

Moving on to the reconstruction, using transmission mean and variance from a single bichromatic illumination, we can generate reconstruction volumes which correspond to the attenuation of the object at each of the two energy bins, then extract the density and atomic number of the object on a per-pixel basis. Let transmitted intensity data at energy E_0 and E_1 along a line from the source to the detector parametrized by L be $I_0(L; E_0)$ and $I_0(L; E_1)$ without the object, and $I(L; E_0)$ and $I(L; E_1)$ with the object. From these we can extract the projected attenuation at each energy, $A_0(L)$ and $A_1(L)$, using Eq. (3). This gives

$$A_j(L) = \int_L \mu(\mathbf{x}; E_j)\, ds = -\ln\left(\frac{I(L; E_j)}{I_0(L; E_j)}\right),$$

for $j = 0$ or $j = 1$. However, the transmission mean and variance, which we observe, both contain a mixture of $A_0(L)$ and $A_1(L)$. Nevertheless, these single-energy projected attenuation data can be extracted by solving a simple set of linear equations.

Assume that the spectral distribution is known for both the mean ($\overline{S}$) and the variance data ($\check{S}$). The spectral distribution for the mean has the form

$$\overline{S}(E) = \overline{\lambda}\delta(E - E_0) + (1 - \overline{\lambda})\delta(E - E_1),$$

for $0 < \overline{\lambda} < 1$, and $\delta(\eta)$ is the usual Dirac delta function. As described in Sec. III D, the corresponding spectrum for the

variance data, found according to Eq. (13), is

$$\check{S}(E) = \check{\lambda}\delta(E - E_0) + (1 - \check{\lambda})\delta(E - E_1),$$

where $\check{\lambda} = \bar{\lambda}/(\bar{\lambda}E_0 + (1 - \bar{\lambda})E_1)$. The mean and variance transmission measurements given this bichromatic spectrum are therefore

$$\overline{T}(L) = \bar{I}(L)/\bar{I}_0 L$$

$$= \bar{\lambda}\exp^{-A_0(L)} + (1 - \bar{\lambda})\exp^{-A_1(L)}, \qquad (19)$$

$$\check{T}(L) = \check{I}(L)/\check{I}_0 L$$

$$= \check{\lambda}\exp^{-A_0(L)} + (1 - \check{\lambda})\exp^{-A_1(L)}. \qquad (20)$$

Solving the above equations for $A_0(L)$ and $A_1(L)$ gives the single energy projected attenuation of the object:

$$A_0(L) = -\ln\left(\frac{(1 - \check{\lambda})\overline{T}(L) - (1 - \bar{\lambda})\check{T}(L)}{(1 - \check{\lambda})\bar{\lambda} - (1 - \bar{\lambda})\check{\lambda}}\right), \qquad (21)$$

$$A_1(L) = -\ln\left(\frac{\check{\lambda}\overline{T}(L) - \bar{\lambda}\check{T}(L)}{\check{\lambda}(1 - \bar{\lambda}) - \bar{\lambda}(1 - \check{\lambda})}\right). \qquad (22)$$

Once these projected attenuation data have been calculated, the dual-energy reconstruction process can proceed in the conventional way (a more detailed description is given in Sec. C 1 of Appendix C). Alternatively, the Appendix also shows that the projected material properties can be extracted and reconstructed using conventional reconstruction methods. A third way of proceeding is to perform conventional iterative reconstruction directly on $A_0(L)$ and $A_1(L)$. Since both $A_0(L)$ and $A_1(L)$ are at a single energy, there is no beam hardening and the reconstructed images are free from beam-hardening artifacts. Material properties can be extracted from these tomograms using Eqs. (C2) and (C3). This is the method employed here.

As before, we carry out Monte Carlo simulations in two dimensions using a line detector. The sample used in this section for simulations consists of a quartz (silicon dioxide), a potassium metal, and white phosphorus rods, all with radius 0.5 cm, imaged with parallel beam x rays. We selected these samples for the simulation because of their distinct atomic number and densities, which makes the results more easily comprehensible, notwithstanding the practicality of placing potassium metal next to white phosphorus. The x rays are equally split between two energy bins, 30 and 60 keV. A total 2000 projection images are simulated with a 500-pixel line detector with a pixel pitch of 28 μm. For each 1D projection measured, 20 000 trials are conducted, and the mean and variance data are calculated from the trials using mean absolute deviation. In each trial, a random number of photons is generated and attenuated using the NIST-XCOM attenuation data [12], and the emerging photons are recorded for each detector pixel. The photon number follows the Poisson distribution with mean of 10 000. They are then used to solve for the monochromatic projected attenuations according to Eqs. (21) and (22), and the solved monochromatic projected attenuations are finally reconstructed using 30 iterations of ordered-subset simultaneous iterative reconstruction technique (SIRT). Finally, the reconstruction result of the monochromatic projected attenuations is used to solve for the density and atomic number using the Alvarez-Macovski

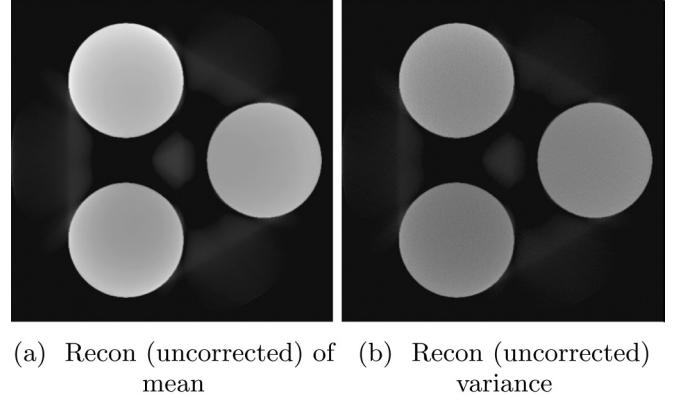(a) Recon (uncorrected) of mean   (b) Recon (uncorrected) variance

FIG. 8. Conventional reconstruction of the bichromatic data. The materials are, clockwise from top, phosphorus, quartz, and potassium; grayscale is [0, 1.64] for both.

equation [Eq. (4)]. To reduce noise, which is exacerbated by the linear equation solving, we applied a median filter with a 7×7 kernel on the reconstruction result of the monochromatic projected attenuations before and after we solved the density values. This explains the smooth appearance of the density and atomic number images when compared to the noisy attenuation reconstruction images.

For comparison, we reconstructed the variance and mean directly using conventional methods and the results are given in Fig. 8; here both the reconstruction of the mean and variance image are marred by beam hardening, and the effect is stronger in the reconstruction of the mean image. The attenuation values of the three materials blend together so it is very difficult to distinguish the materials with confidence. The results of the conventional reconstruction of the separated monochromatic attenuation $A_0(L)$ and $A_1(L)$ are given in Fig. 9. Although both reconstructions are marred by high levels of noise, which originates in the noisy variance data and is amplified after solving the linear equations to find $A_0(L)$ and $A_1(L)$, beam hardening has been eliminated in both reconstructions. The histograms [Figs. 9(b) and 9(d)] also show that the reconstruction is quantitative: the peaks of the histograms correspond to the theoretical attenuation of the materials at both 30 and 60 keV (vertical lines). In the reconstruction of the attenuation tomograms the values of potassium blend with those of phosphorus at 30 keV [Fig. 9(b), left peak, and Table I, column 3] and with that of quartz at 60 keV [Fig. 9(d), right peak, and Table I, column 4], so it is still difficult to distinguish the materials using only one reconstruction. On the other hand, we can easily distinguish the three materials

TABLE I. Material properties for the bichromatic simulation. Units are g cm^{-3} for density ρ and cm^{-1} for attenuation coefficient μ. Density values are reference values. Atomic numbers are calculated from the formula in Ref. [11]. Attenuation coefficients are from NIST [12].

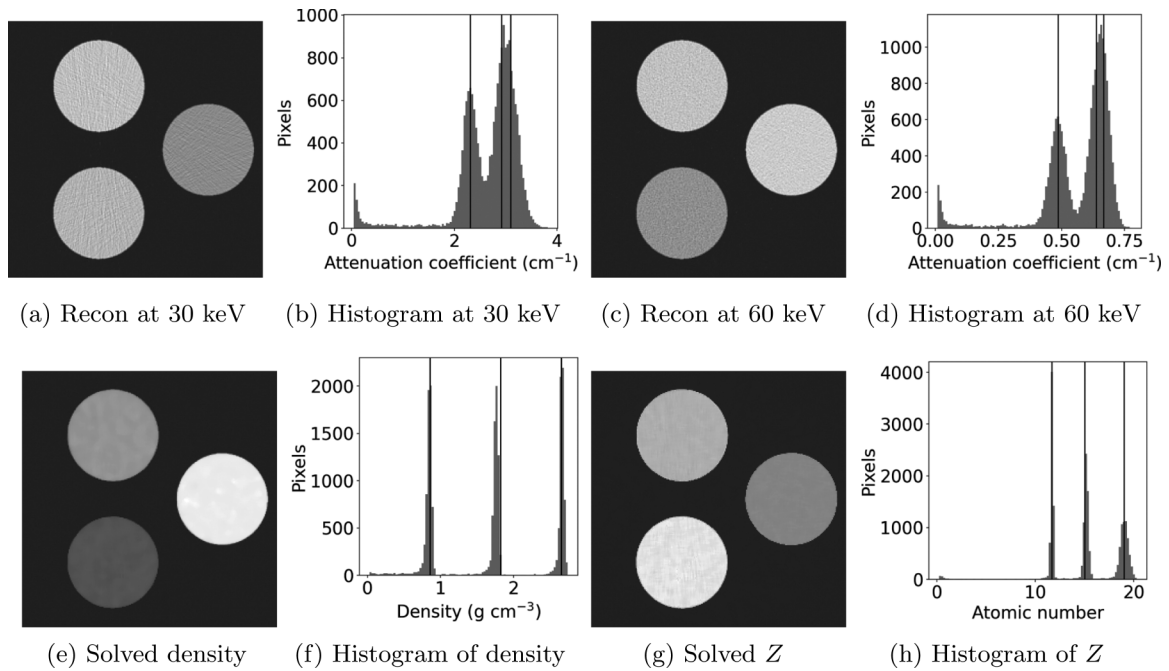| Name	ρ	Z	μ (30 keV)	μ (60 keV)
Potassium	0.86	19.00	2.92	0.49
Phosphorus	1.82	15.00	3.10	0.64
Quartz	2.65	11.65	2.31	0.67

FIG. 9. (a) Conventional reconstruction of $A_0(L)$, the grayscale values are [0, 3.82]; (b) its histogram; (c) Conventional reconstruction of $A_1(L)$, the grayscale values are [0, 0.78] (d) its histogram; (e) Density volume generated from the attenuation reconstructions, the grayscale values are [0, 2.74]; (f) its histogram; (g) Atomic number volume generated from the attenuation reconstructions, the grayscale values are [0, 20.3]; (h) its histogram.

using either the solved density [Fig. 9(e)] or the solved atomic number [Fig. 9(g)] images. We also observe good quantitative agreement as the expected peaks of the histograms [Figs. 9(f) and 9(h)] fall at the locations of the correct values indicated by the vertical lines (see Table I). This demonstrates that our method is indeed capable of extracting quantitative material data, at least in the bichromatic case, by treating the variance image on the same footing as the mean image.

2. Polychromatic illumination

For polychromatic x rays with more than two energy bins, dual-energy reconstruction is more complicated. The simulation variance and mean transmission images of the aluminum and marble were collected with a polychromatic x-ray spectrum that has maximum energy of 80 keV. The variance and mean transmission are shown in Fig. 10. And we note the similarity in the ratio between the variance and the mean transmission [Fig. 10(c)] between this case and the bichromatic case. The histogram of the variance mean ratio is given in Fig. 10(d); in comparison with the bichromatic case, we note the presence of a lower peak which corresponds to the x ray which did not pass through the object, since it has value equal to the mean energy of the original x-ray beam (38.5 keV).

The conventional iterative procedure for dual-energy CT is used for the tomographic reconstruction: x rays at two different spectra are obtained via filtering or different x-ray tube settings; the object is then illuminated with each of the two x-ray spectra, which are known beforehand. In every iteration of the reconstruction the attenuation images at two different (monochromatic) energies are used to solve for the

two components of the Alvarez-Macovski model. They are then projected and used to generate polychromatic intensity data which are compared with the actual sinograms; the difference is then backpropagated. We use the variance data as the higher-energy sinogram, and the mean data as the lower-energy sinogram.

The simulation method used for the polychromatic case is modeled closely on the previous simulations presented in Secs. V A and V C 1. As before, Monte Carlo simulation in two dimensions using a line detector is used. The sample consists of aluminum, sulfur, periclase (magnesium oxide), and rutile (titanium oxide) rods, all with radius 0.5 cm, imaged with parallel beam x rays. The x rays are generated from a tungsten target with electrons accelerated to 80 keV, and the energy bins have a width of 1 keV. A total of 2000 projection images are simulated with a 500-pixel line detector with a pixel pitch of 28 μm. For each 1D projection measured, 500 trials are conducted, and the mean and variance data are calculated from the trials using mean absolute deviation. In each trial, a random number of photons is generated and attenuated using the NIST-XCOM attenuation data [12], and the emerging photons are recorded for each detector pixel. The photon number follows the Poisson distribution with mean of 10 000. The mean and variance projection are given in Fig. 10, along with their ratio and the histogram of the ratio.

Using the projections shown in Figs. 10(a) and 10(b), we can carry out conventional, single-energy iterative reconstruction (15 iterations of ordered-subset simultaneous iterative reconstruction technique (SIRT) [19]), and the results are given in Fig. 11. The reconstruction of the variance image
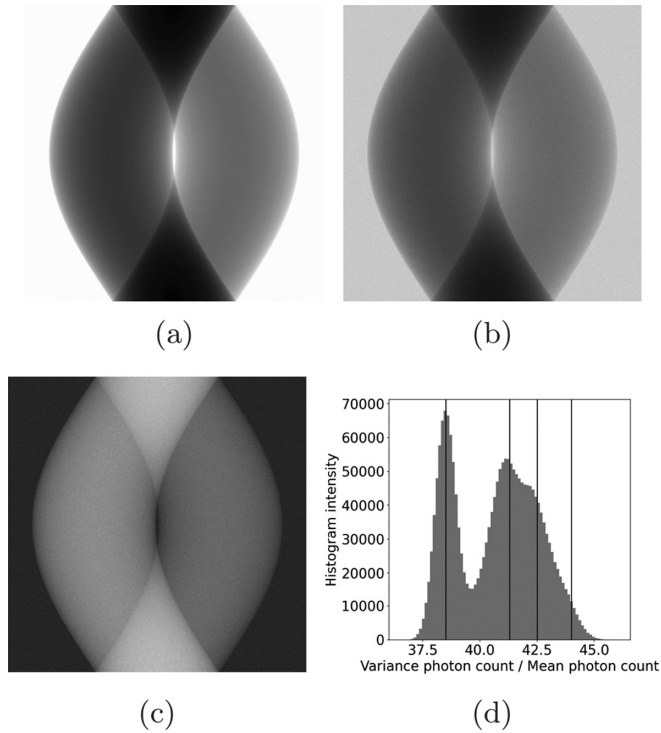
(a)

(b)

(c)

(d)

FIG. 10. (a) Mean intensity, grayscale [213346, 316401], and (b) variance intensity, grayscale [8934554, 12824889], projection images of polychromatic simulation. (c) Their ratio, with grayscale [36.5, 46.1]. (d) Histogram of the ratio; the vertical lines indicate the mean energy of the x ray (1) that did not pass through the object, (2) after it has passed through the center of the aluminum, (3) after it has passed through the center of marble, and (4) and after it has passed through the center of both.

[Fig. 11(a)] has lower attenuation values than the reconstruction of the mean image [Fig. 11(b)], and the mean image has significant beam hardening present, for reasons already mentioned.

Dual-energy reconstruction is then carried out using the variance and mean data. This (15 iterations of ordered-subset SIRT) generates two attenuation reconstruction volumes,

(a) Recon (uncorrected) of mean
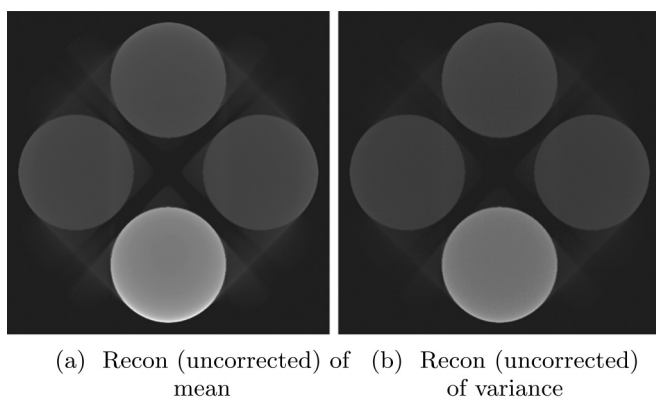
(b) Recon (uncorrected) of variance

FIG. 11. Conventional reconstruction of the polychromatic data. The materials are, clockwise from top, sulfur, aluminum, rutile, and periclase; grayscale is [0, 6.92] for both.

TABLE II. Material properties for the polychromatic simulation. Units are g cm^{-3} for density ρ and cm^{-1} for attenuation coefficient μ. Density values are reference values. Atomic numbers are calculated from the formula in Ref. [11]. Attenuation coefficients are from NIST [12].

Name	ρ	Z	μ (38.5 keV)	μ (45 keV)
Aluminum	2.70	13.00	1.67	1.21
Periclase	3.58	10.78	1.52	1.17
Sulfur	2.07	16.00	2.25	1.53
Rutile	4.52	18.70	7.16	4.77

which are given in Figs. 12(a) and 12(c). Compared to the single-energy reconstruction, the two attenuation volumes generated by dual-energy reconstruction are free from artifacts. Furthermore, the actual values of the materials in the dual-energy reconstruction correspond to the attenuation coefficients of the materials at E_0 and E_1 (columns 3 and 4 of Table II). In this sense, the reconstruction is quantitative. By solving the Alvarez-Macovski equation using these two attenuation images, we obtain the density [Fig. 12(e)] and atomic number [Fig. 12(g)] images. Again, noise is amplified during this process, and noise suppression via median filters (with a 7×7 kernel) is used twice before the final image is obtained. There is good agreement between both the solved densities of the materials and the correct values (given as vertical lines in the accompanying histogram and the exact values are given in column 1 of Table II). Similarly, there is also good agreement between the solved effective atomic numbers of the materials and the correct values (column 2 of Table II). These results suggest that quantitative dual-energy reconstruction is possible using variance and mean data.

VI. CONCLUSIONS AND FUTURE WORK

We have demonstrated that, if shot noise from incoming photon detection is the dominant cause of measurement noise (modeled as a Poisson distribution), then it is possible to extract spectral information from photon detectors that measure aggregate intensity. This enhances our understanding about (i) the capabilities of these existing detectors and (ii) the significance of the variance data. Specifically for the case of polychromatic x-ray radiography and tomography, the *variance* of transmission data provides distinct information when compared to the *mean* of the transmission data. The variance data are a form of conventional transmission data, similar to the mean data but imaged with a harder spectrum; they can be used in a completely independent manner to perform radiography and tomography.

Transmission variance combined with the more conventional transmission mean yields knowledge of the x-ray spectrum; the ratio of variance to mean is a direct measurement of beam hardening. This knowledge can be used to perform beam-hardening correction. We present two such methods: (i) directly from these measurements, assuming attenuation by photoelectric absorption only, and (ii) using these measurements to automatically calibrate a linearization curve.

Given knowledge of the input x-ray spectrum, the transmission mean and variance measurements can serve as the

(a) Recon at 38.5 keV   (b) Histogram at 38.5 keV   (c) Recon at 45 keV   (d) Histogram at 45 keV

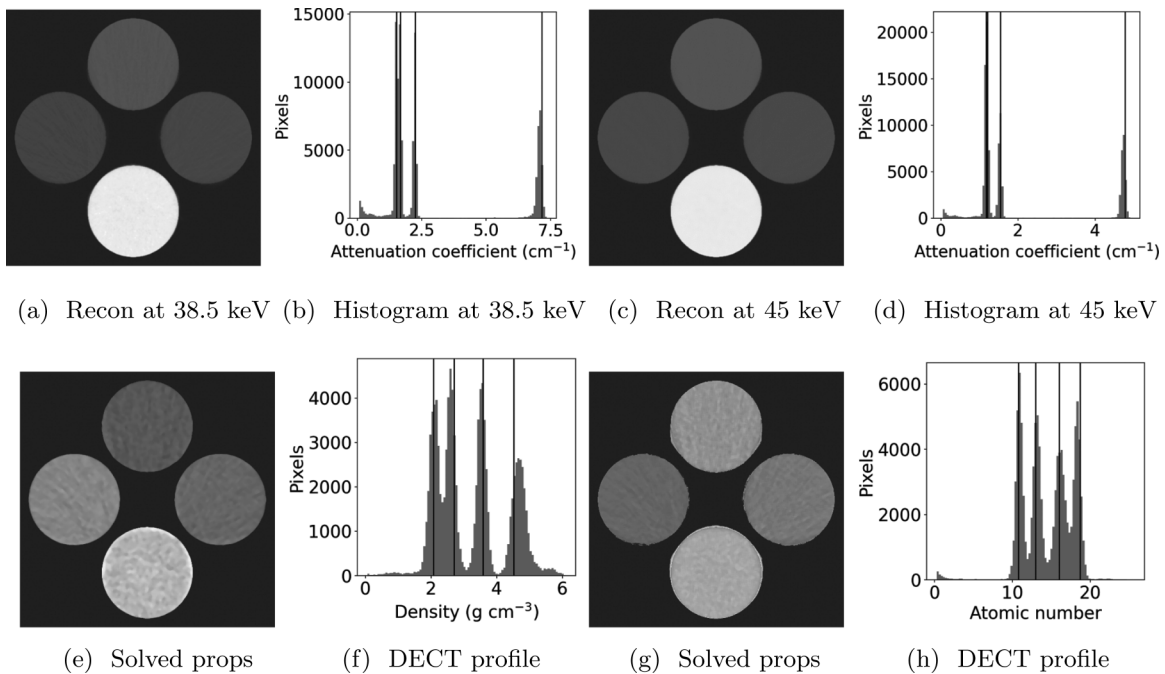(e) Solved props   (f) DECT profile   (g) Solved props   (h) DECT profile

FIG. 12. (a) DECT reconstruction using the mean and variance transmissions, at 38.5 keV, grayscale is [0, 7.36]; (b) its histogram; (c) DECT reconstruction using the mean and variance transmissions, at 45 keV, grayscale is [0, 4.92]; (d) its histogram; (e) Density volumes generated from the dual-energy reconstruction volumes, grayscale is [0, 6.10]; (f) its histogram; (g) Atomic number volumes generated from the dual-energy reconstruction volumes, grayscale is [0, 25.71]; (h) its histogram.

low- and high-energy measurements in DECT. We carried out simulations for the case of bichromatic and polychromatic x-ray spectra and obtained quantitative results without requiring the use of a second x-ray spectrum or spectrum-resolving detectors. We retrieved attenuation values at two energies and then, using the Alvarez-Macovski x-ray attenuation model, we derived density and atomic number of the materials in the sample.

Despite these achievements, we recognize this variance method comes with its share of limitations. First, the typical procedure for taking measurements in XCT needs to be modified: extra acquisition time may be required to collect enough readings to generate sufficient x-ray statistics. Accurate estimation of variance is also challenging in practice, so we utilized mean absolute deviation which is a robust on-the-fly method for variance calculation. Second, the variance data are inherently noisier than the mean data, and the solutions to generate density and atomic number data are sensitive to noise; this necessitates the use of regularization during and after the iterative tomographic reconstruction.

The first priority for any future work lies in achieving the dual-energy quantitative reconstruction with experimental data. We do not yet know the full range of issues that would need to be resolved before this can be achieved, but it would certainly include the two challenges listed in the previous paragraph. In particular, the length of acquisition to obtain a reasonable tomogram needs to be investigated. This is linked with the issue of denoising, which is itself a large and complex issue. It may be pertinent to choose the best denoising method among the available options and integrate it inside the reconstruction. Furthermore, there are issues specific to the quality of experimental data. In our simulations

we have discarded scatter and assumed a single x-ray source, whereas experiments conducted with laboratory-based x rays are frequently marred by x-ray scatter. There are also issues with the nonhomogeneity of the source, such as uneven flux, presence of secondary sources, etc. Depending on the severity, they may need to be dealt with in some way before accurate quantitative analysis can be achieved. On a more positive note, we hope our simulations and experiments have proven the plausibility of this method, and future developments addressing these (by no means insurmountable) issues should improve the practicality of the method.

Finally, we note that although our application of these new concepts focused on x-ray tomography, we used general principles that may be more broadly applicable across many fields. It is not only relevant to the detection of electromagnetic radiation, but also applies to any scenarios involving discrete events with shot noise measured by an aggregate (or bucket) detector. We hope that our endeavor encourages this new way of thinking and brings forth applications in other areas as well.

APPENDIX A: DETECTOR STATISTICS

The probability of x-ray photons' registry in a pixel follows a Poisson distribution, the expectation value of which in tomographic contexts is primarily determined by source output, attenuations of intervening materials, and the stopping

power of absorbing material in the detector; it is a function of x-ray photon energy E (see Eq. 7 of Ref. [1]). For every photon thus received, it will contribute some of the x-ray photon's energy towards an eventual intensity signal, via lossy transduction mechanisms that are specific to the detector [3]. Provided that proportional relationships are carried through all transductions, gains, and other aspects of the signal chain, the final (pileup) intensity will then be proportional to the energy of the impinging x-ray photons (see Eq. 1 of Ref. [1]). In this work the signal chain's lumped proportionality constant is denoted $\Gamma(E)$, which observes its likely dependence on the x-ray photon energy (for potentially very many reasons within the chain). It is important to note that the Poisson expectation number of photons and the $\Gamma(e)$ function have no relationship to each other. Next, intensity variance arises from variation in the number of x-ray photons. Intensity deviations due to that Poisson variability are, like the intensity itself, proportional to $\Gamma(E)$, and otherwise proportional to the square root of the Poisson expectation number (see Eq. 2 of Ref. [1]). For monochromatic x-ray photons, observable intensity variance divided by observable mean intensity is then simply the product of the x-ray photon energy and the $\Gamma(E)$ function (see Eq. 3 of Ref. [1]). In polychromatic cases, the intensity variance and mean remain informative in demonstrable ways (see Eq. 4 ad Figs. 2 and 4 of Ref. [1]) that relate to the dispersion of the spectrum (see Eq. 23 and Fig. 3 of Ref. [1]). The key feature is that the variance of observable intensity and the mean of observable intensity are together informative about the x-ray photon energies and their spectra, regardless of pileup of Poisson-distributed events in proportional detectors. Since a relationship ties those things (see Eq. 4 of Ref. [1]), efforts to model spectra have one less degree of freedom, which in effect applies to each voxel of a tomogram. The constraint is potentially very useful indeed given adequately descriptive models, especially where redundant information may in effect provide a ready supply of variance- and mean-related information. This situation exists among the many projections typically used in tomographic reconstructions. It is also readily amenable to Monte Carlo verifications and simulations.

In the present work the preceding aspects employ the following notations: the intensity in a given pixel may be written $\sum_i n_i E_i \Gamma(E_i)$, where n_i photons have energy E_i; the mean reading is $\sum_i \bar{n}_i E_i \Gamma(E_i)$; and the total quadrature-added intensity variance is $\sum_i \bar{n}_i E_i^2 \Gamma^2(E_i)$. The variance of detector readings carries information distinct from the mean, and that the distinction relates to the spectrum. We explored the implications in the body of this paper.

What the Γ function is (and is not) is more clearly delineated in the beginning of Sec. I. We have not sought a parametric description of Γ beyond observing that it is expected to be a function of x-ray photon energy in some detector-specific way. A reason for refraining is that we often use different detectors, in which signal transduction follows different courses, and in signal chains that end users are often obliged to view as a "black box" through multiple tiers of manufacturing industry, in their capacity as purchasing customers. As such, attempts at parametrization of $\Gamma(E)$ would only add obfuscating detail and speculations to this work, where we shortcut to the key property of all energy-integrating

detectors, namely, that the original photon's energy is ultimately retained in some proportional sense, in the sum or integral in a pileup situation. [Efforts to parametrize and optimize $\Gamma(E)$ are a subject of studies in detector manufacturing industries and relevant bodies of work (e.g., Ref. [3]); via direct-detection detectors they reach their ultimate expression in low temperature thermal detectors, the extended awareness and use of which indeed served as a background for the present work (e.g., Refs. [16,22])].

APPENDIX B: ROBUST DETERMINATION OF VARIANCE

The standard method of estimating variance is as follows: given n measurements taken sequentially in time, first calculate the sample mean as

$$\bar{x} = \frac{1}{n} \sum_{i=1}^{N} x_i,$$

where i is the index of the measurement in the sequence. Then the sample variance is

$$\check{x} = \frac{1}{n} \sum_{i=1}^{N} (\bar{x} - x_i)^2.$$

There are also methods to calculate the mean and variance in a cumulative fashion while gathering the measurement, and complete the calculation in one pass. However, both the on-the-fly and *post hoc* methods are quadratic, which causes them to be highly sensitive to extreme outliers. This can be improved with a second pass over the data, recalculating the mean and then variance by ignoring all measurements more than a few (initial) standard deviations from the (initial) mean.

This sensitivity can also be reduced, with a single pass of the measurements, by using the mean absolute deviation (MAD). For Gaussian distributions, the MAD scaled by $\sqrt{\pi/2}$ gives the standard deviation [23]; we therefore have

$$\check{x} = \frac{\pi}{2} \left(\frac{1}{n} \sum_{i=1}^{N} |\bar{x} - x_i| \right)^2.$$

However, we found that this measurement was still unstable, particularly at edges of the specimen projection image, due to specimen movement and flux (or mean) variation. The instability can be reduced by calculating a *running* mean and variance (with the complication of parameter value optimization).

These slow variations can be overcome with a single pass of the measurements by calculating the variance between adjacent measurements. Here we are actually calculating the variance of the difference of two Gaussian distributions. Using the MAD technique described above, we arrive at

$$\check{x} = \frac{\pi}{4} \left(\frac{1}{n-1} \sum_{i=2}^{N} |x_i - x_{i-1}| \right)^2.$$

Also observe that this method does not require an estimate of the mean for computation and can therefore be computed on the fly as with mean estimation.

APPENDIX C: DUAL-ENERGY ITERATIVE TOMOGRAPHIC RECONSTRUCTION

Several methods for iterative reconstruction of dual-energy XCT data exist in the literature (e.g., Refs. [24,25]). Here we provide details of the method used in Secs. V C 1 and V C 2 which is based on minor modifications to the single-energy polychromatic iterative reconstruction method presented in Ref. [13].

1. Iterative tomographic reconstruction

The measurement process of XCT can be expressed by the linear equation

$$\mathbf{A}\mathbf{x} = \mathbf{b}.$$

Here $\mathbf{x}$ is an N-pixel representation of the attenuation of the object to be reconstructed, $\mathbf{b}$ is the M linearized (via negative logarithm) measurements that are modeled as line integrals through $\mathbf{x}$, and $\mathbf{A}$ is an $M \times N$ system matrix that represents the projection process, i.e., M line integrals though the N-pixel object.

Iterative reconstruction (IR) methods use various optimization techniques to solve for $\mathbf{x}$ given $\mathbf{b}$ and $\mathbf{A}$ [8]. One of the simplest forms of IR is the Landweber method [26]. Given a current estimate of the attenuation of the object, $\mathbf{x}^k$, the updated estimate $\mathbf{x}^{k+1}$ is found as

$$\mathbf{x}^{k+1} = \mathbf{x}^k + \lambda \mathbf{A}^T (\mathbf{b} - \mathbf{A}\mathbf{x}^k). \tag{C1}$$

Here λ is a regularization parameter, typically on the order of $1/\eta\omega$ where η is the image dimension in voxels, e.g., $\eta = \sqrt{N}$ for a square image, and ω is the average number of rays through voxel, e.g., typically $\omega = M/\eta$. Landweber iteration is a form of gradient descent and minimizes the L^2 norm of the residual, $\mathbf{r} = \mathbf{b} - \mathbf{A}\mathbf{x}$. Algorithm 1 gives an n-iteration pseudocode example starting with a zero estimate.

Algorithm 1 Landweber iteration.

```
input  : Linearised projection b, Landweber
           parameter λ
output: Reconstructed attenuation x

x ← 0;
for k ← 1 to n do
    b̃ ← Ax;
    r ← b − b̃;
    x ← x + λAᵀr;
end
```

2. Extracting material properties from dual-energy data

Let us first consider the simplest case of dual-energy XCT with two experiments performed with monochromatic illumination at x-ray energies E_0 and E_1. Given the two linearized (via negative logarithm) measurements, $\mathbf{b}_0$ and $\mathbf{b}_1$, we can extract the material properties of density, ρ, and effective atomic number, Z, through Eq. (4).

We perform Landweber iteration to recover the attenuation of the object at each energy, $\mathbf{x}_0$ and $\mathbf{x}_1$. Then at each voxel position of the object representation, i for $0 \leqslant i < N$, we can

compute $\rho_i Z_i^{3.2}$ and ρ_i by rearranging the two forms of Eq. (4) at energies E_0 and E_1 as follows:

$$\rho_i Z_i^3 = \frac{\beta f_{\mathrm{KN}}(E_1) x_{0,i} - \beta f_{\mathrm{KN}}(E_0) x_{1,i}}{\frac{\alpha}{E_0^3} \beta f_{\mathrm{KN}}(E_1) - \frac{\alpha}{E_1^3} \beta f_{\mathrm{KN}}(E_0)}, \tag{C2}$$

$$\rho_i = \frac{\frac{\alpha}{E_0^3} x_{1,i} - \frac{\alpha}{E_1^3} x_{0,i}}{\frac{\alpha}{E_0^3} \beta f_{\mathrm{KN}}(E_1) - \frac{\alpha}{E_1^3} \beta f_{\mathrm{KN}}(E_0)}. \tag{C3}$$

3. Polychromatic projection given material properties

Given knowledge of a spectral distribution, $S(E)$ (and the corresponding AM constants α and β), the material property distributions $\boldsymbol{\rho}$ and $\boldsymbol{\rho}\mathbf{Z}^3$ calculated above allow us to simulate the polychromatic projection. Let us first project the material properties: $\boldsymbol{\phi} = \mathbf{A}\boldsymbol{\rho}\mathbf{Z}^3$ and $\boldsymbol{\theta} = \mathbf{A}\boldsymbol{\rho}$. The projected attenuation of the object at energy E can be determined via Eq. (5) as follows:

$$\widetilde{\mathbf{b}}(E) = \frac{\alpha}{E^3}\boldsymbol{\phi} + \beta f_{\mathrm{KN}}(E)\boldsymbol{\theta}. \tag{C4}$$

As was explained in Sec. II A, the linearized polychromatic measurements, $\widetilde{\mathbf{b}}$, cannot be formed as the sum of $\widetilde{\mathbf{b}}(E)$ over the spectrum, but rather the negative logarithm of the sum of transmission over the spectrum, i.e.,

$$\widetilde{\mathbf{b}} = -\ln(\mathbf{T})$$

$$= -\ln\left(\sum_E S(E) \exp[-\widetilde{\mathbf{b}}(E)]\right). \tag{C5}$$

Algorithm 2 Dual-Energy Landweber iteration.

```
input  : Linearised projections b₀ and b₁, spectra
           S₀(E) and S₁(E), AM parameters α and
           β, Landweber parameter λ.
output: Reconstructed attenuation at two
           energies, x₀ and x₁.

x₀ ← 0;
x₁ ← 0;
for k ← 1 to n do
    ρZ³ ← EqC2(x₀, x₁);
    ρ ← EqC3(x₀, x₁);
    φ ← AρZ³;
    θ ← Aρ;
    T₀ ← 0;
    T₁ ← 0;
    for E ← 1 to Eₘₐₓ do
        b̃(E) ← (α/E³)φ + βf_KN(E)θ;
        T₀ ← T₀ + S₀(E) exp[−b̃(E)];
        T₁ ← T₁ + S₁(E) exp[−b̃(E)];
    end
    r₀ ← b₀ + log(T₀);
    r₁ ← b₁ + log(T₁);
    x₀ ← x₀ + λAᵀr₀;
    x₁ ← x₁ + λAᵀr₁;
end
```

4. Dual-energy polychromatic iterative tomographic reconstruction

The above components provide the foundation for extracting material properties from polychromatic dual-energy projection measurements in iterative reconstruction. Given spectral distributions, $S_0(E)$ and $S_1(E)$, and the associated polychromatic linearized measurements (via negative logarithm of transmission), $\mathbf{b}_0$ and $\mathbf{b}_1$, we want to determine $\mathbf{x}_0 = \mathbf{x}(E_0)$ and $\mathbf{x}_1 = \mathbf{x}(E_1)$ where $E_0 = \mathrm{Mean}[S_0(E)]$ and $E_1 = \mathrm{Mean}[S_1(E)]$ are the mean energies of $S_0(E)$, $S_1(E)$, respectively. Starting with a current estimate, $\mathbf{x}_0^k$ and $\mathbf{x}_1^k$, we first determine $\rho \mathbf{Z}^3$ through Eq. (C2) and $\boldsymbol{\rho}$ through Eq. (C3). These volumes are projected to give $\boldsymbol{\phi}$ and $\boldsymbol{\theta}$. These provide the basis for determining the estimate of projected attenuation of the object at energy E, $\widetilde{\mathbf{b}}(E)$, as described in Eq. (C4). The spectrally weighted sum of transmission, i.e., $\exp[-\widetilde{\mathbf{b}}(E)]$, at each energy, E, gives the total transmission for each spectrum, $\mathbf{T}_0$ and $\mathbf{T}_1$. The linearized projection estimates are then calculated as $\widetilde{\mathbf{b}}_j = -\ln(\mathbf{T}_j)$, for j in $\{0,1\}$ according to Eq. (C5). The residuals, $\mathbf{r}_0$ and $\mathbf{r}_1$, as well as new estimates $\mathbf{x}_0^{k+1}$ and $\mathbf{x}_1^{k+1}$ are then computed according to the Landweber method described in Algorithm 1. An example n-iteration pseudocode of this entire process is outlined in Algorithm 2.

There are of course many other methods to perform single-energy IR, and most can be generalized to dual-energy IR. The objective of this Appendix is to provide a convenient and concise explanation of the dual-energy IR used in this paper. Finally, we wish to note that the set of linear equations can be solved in projection space for $\int_L \rho(\mathbf{x})\,ds$ and $\int_L \rho(\mathbf{x})Z^{3.2}(\mathbf{x})\,ds$. It is then possible to carry out tomographic reconstruction on both $\rho(\mathbf{x})$ and $\rho Z^{3.2}(\mathbf{x})$ directly using conventional tomographic reconstruction techniques.

[1] W. K. Fullagar, M. Paziresh, S. J. Latham, G. R. Myers, and A. M. Kingston, The index of dispersion as a metric of quanta—unravelling the Fano factor, Acta Crystallogr., Sect. B: Struct. Sci., Cryst. Eng. Mater. **73**, 675 (2017).

[2] I. A. Cunningham and R. Shaw, Signal-to-noise optimization of medical imaging systems, J. Opt. Soc. Am. A **16**, 621 (1999).

[3] I. A. Cunningham, M. S. Westmore, and A. Fenster, A spatial-frequency dependent quantum accounting diagram and detective quantum efficiency model of signal and noise propagation in cascaded imaging systems, Med. Phys. **21**, 417 (1994).

[4] B. R. Whiting, P. Massoumzadeh, O. A. Earl, J. A. O'Sullivan, D. L. Snyder, and J. F. Williamson, Properties of preprocessed sinogram data in x-ray computed tomography, Med. Phys. **33**, 3290 (2006)

[5] D. G. Morgenthaler, R. A. Brooks, and A. J. Talbert, Noise factor of a polyenergetic x-ray beam in computed tomography, Phys. Med. Biol. **25**, 251 (1980)

[6] C. Cai, T. Rodet, S. Legoupil, and A. Mohammad-Djafari, A full-spectral Bayesian reconstruction approach based on the material decomposition model applied in dual-energy computed tomography, Med. Phys. **40**, 111916 (2013)

[7] S. Yoon, S. A. Makiharju, J. A. Fessler, and S. L. Ceccio, Image reconstruction for limited-angle electron beam x-ray computed tomography with energy-integrating detectors for multiphase flows, IEEE Trans. Comput. Imaging **4**, 112 (2018)

[8] J. Nuyts, B. D. Man, J. A. Fessler, W. Zbijewski, and F. J. Beekman, Modelling the physics in the iterative reconstruction for transmission computed tomography, Phys. Med. Biol. **58**, R63 (2013).

[9] R. E. Alvarez and A. Macovski, Energy-selective reconstructions in x-ray computerised tomography, Phys. Med. Biol. **21**, 733 (1976).

[10] O. Klein and Y. Nishina, The scattering of light by free electrons according to Dirac's new relativistic dynamics, Nature (London) **122**, 398 (1928).

[11] M. Paziresh, A. M. Kingston, S. J. Latham, W. K. Fullagar, and G. M. Myers, Tomography of atomic number and density of materials using dual-energy imaging and the Alvarez and Macovski attenuation model, J. Appl. Phys. **119**, 214901 (2016).

[12] M. J. Berger, J. H. Hubbell, S. M. Seltzer, J. Chang, J. S. Coursey, R. Sukumar, D. S. Zucker, and K. Olsen, XCOM: Photon Cross Section Database, 2010, https://dx.doi.org/10.18434/T48G6X.

[13] Q. Yang, W. Fullagar, G. Myers, S. Latham, T. Varslot, A. Sheppard, and A. Kingston, X-ray attenuation models to account for beam hardening in computed tomography, Appl. Opt. **59**, 9126 (2020).

[14] M. S. and A. C. Kak, *Principles of Computerized Tomographic Imaging* (IEEE, Piscataway, NJ, 1988).

[15] T. R. C. Johnson, Dual-energy CT: General principles, Am. J. Roentgenol. **199**, S3 (2012).

[16] W. K. Fullagar, J. Uhlig, U. Mandal, D. Kurunthu, A. E. Nahhas, H. Tatsuno, A. Honarfar, F. P. Gustafsson, V. Sundström, M. R. J. Palosaari, K. M. Kinnunen, I. J. Maasilta, L. Miaja-Avila, G. C. O'Neil, Y. I. Joe, D. S. Swetz, and J. N. Ullom, Beating Darwin-Bragg losses in lab-based ultrafast x-ray experiments, Struct. Dyn. **4**, 044011 (2017).

[17] Pixium RF 4343 - Pixium RF 4343 F5 - Pixium RF 4343FL, https://www.thalesgroup.com/en/markets/market-specific-solutions/microwave-imaging-sub-systems/medical-imaging/radiography-0 (unpublished).

[18] A. Papoulis, *Probability, Random Variables, and Stochastic Processes*, Communications and Signal Processing (McGraw-Hill, New York, 1991).

[19] H. Erdogan and J. A. Fessler, Ordered subsets algorithms for transmission tomography, Phys. Med. Biol. **44**, 2835 (1999).

[20] K. Lange and R. Carson, EM reconstruction algorithms for emission and transmission tomography, J. Comput. Assist. Tomogr. **8**, 306 (1984).

[21] A. M. Kingston, W. K. Fullagar, G. R. Myers, and A. P. Sheppard, Imaging mean energy of x-ray spectra through intensity variation in radiographs with an example application to beam hardening correction, Microsc. Microanal. **24**, 110 (2018).

[22] W. Fullagar, J. Uhlig, M. Walczak, S. Canton, and V. Sundström, The use and characterization of a backilluminated charge-coupled device in investigations of pulsed x-ray and radiation sources, Rev. Sci. Instrum. **79**, 103302 (2008).

[23] E. M. J. Herrey, Confidence intervals based on the mean absolute deviation of a normal sample, J. Am. Stat. Assoc. **60**, 257 (1965).

[24] X. Dong, T. Niu, and L. Zhu, Combined iterative reconstruction and image-domain decomposition for dual energy CT using total-variation regularization, Med. Phys. **41**, 051909 (2014).

[25] T. P. Szczykutowicz and G.-H. Chen, Dual energy CT using slow kVp switching acquisition and prior image constrained compressed sensing, Phys. Med. Biol. **55**, 6411 (2010).

[26] L. Landweber, An iteration formula for Fredholm integral equations of the first kind, Am. J. Math. **73**, 615 (1951)